THE ASTROPHYSICAL JOURNAL, 450:201–216, 1995 September 1

STAR FORMATION IN THE GEMINI OB1 MOLECULAR CLOUD COMPLEX

JOHN M. CARPENTER,[1,2] RONALD L. SNELL,[2] AND F. PETER SCHLOERB[2]
Five College Radio Astronomy Observatory, Department of Physics and Astronomy,
University of Massachusetts at Amherst, Amherst, MA 01003
Received 1994 December 27; accepted 1995 March 13

ABSTRACT

We have conducted a study of the global star formation activity in the Gem OB1 molecular cloud complex using a combination of molecular line, near-infrared, and far-infrared data. A global survey for CS($J = 2$–1) emission yielded 11 cores with masses $\gtrsim 100\ M_\odot$. These cores are typically elongated along arcs and filaments previously found in a large-scale ^{12}CO and ^{13}CO survey. Based on the morphology of the cores, the association of some filaments with optical H II regions, and comparison of the observations with models of expanding H II regions, we suggest that these massive cores have formed primarily in swept-up shells of molecular gas. At least eight, and possibly 10, of the 11 cores are associated with star formation as traced by the distribution of *IRAS* point sources, and the three cores contained in our near-infrared imaging survey each contain a cluster of stars. The high frequency of star formation associated with the cores suggests that star formation in massive dense cores begins soon after the core is formed and that new cores must be continually formed if star formation is to continue in the Gem OB1 complex. A systematic survey in CS of 58 *IRAS* sources with far-infrared colors characteristic of young stellar objects indicated that the more luminous *IRAS* sources tend to be associated with more massive cores. This correlation suggests that more massive cores generally form massive stars, although we cannot determine from these data if this is an environmental or statistical effect. Our near-infrared and CS results suggest that dynamical evolution of the clusters and destruction of the cores are important effects to consider when contrasting the properties of different regions. A qualitative model for the Gem OB1 complex is proposed to explain these observations in which the primary mechanism for the formation of the massive dense cores is through the external compression of the molecular gas. The dense cores will generally form clusters of stars that rapidly disperse after the dense core is dissipated. The continual production of dense cores is provided for by the constant interactions of the molecular gas with energetic phenomena in the immediate environment.

Subject headings: H II regions — infrared: stars — ISM: individual (Gemini OB1) — ISM: molecules — stars: formation

1. INTRODUCTION

Recent near-infrared imaging surveys of molecular clouds have revealed the presence of numerous stellar clusters embedded within dense molecular cores. In all censuses, these clusters represent a significant component of recent star formation activity in molecular clouds (Lada, Strom, & Myers 1994) despite occupying a small fraction of the total cloud area. Understanding how dense cores and clusters form and why they form in certain regions of molecular clouds and not others, however, has proven to be a more difficult task. With the increasing ability to efficiently map cloud complexes at both millimeter and infrared wavelengths, the global structure and star formation activity in cloud complexes can now be studied in a more systematic manner than previously possible (e.g., Lada, Bally, & Stark 1991a; Lada et al. 1991b), with the hope that such studies can begin to reveal the conditions required to form cores and stellar clusters. In this paper, we present the results of such a study of the Gem OB1 molecular cloud complex through analysis of far-infrared *IRAS* data, near-infrared images, and molecular line observations.

A detailed description of the large-scale structure of the Gem OB1 cloud complex based upon extensive ^{12}CO and ^{13}CO observations was presented by Carpenter, Snell, & Schloerb (1995, hereafter Paper I). Briefly, the Gem OB1 cloud complex extends over 32 deg^2 at a distance of $\sim$2 kpc and contains $\sim 3.2 \times 10^5\ M_\odot$ of molecular material. With a spatial coverage of 177 pc $\times$ 221 pc at a sampling of 0.48 pc, these maps provide one of the most detailed examinations of the global structure of a molecular cloud complex to date. The optical H II regions within the Gem OB1 cloud complex include Sh 247, Sh 252, Sh 254–258, and BFS 52. The most striking morphological features of the molecular gas are the numerous arcs and filaments present on spatial scales extending from a few parsecs to more than 35 pc. Some of these arc-shaped structures are found around extended optical H II regions, which suggests that these features represent swept-up shells of molecular gas. Most of the arcs and filaments, though, are not directly associated with optical nebula. However, the morphology and kinematics of these structures strongly imply that energetic events, perhaps associated with massive star formation, are responsible for their origin. Given this general understanding of the structure and properties of the molecular gas in the Gem OB1 cloud complex, these maps present an opportunity to correlate the spatial distribution of star-forming regions with the structure of the molecular gas to determine where stars form and how the properties of the young stars depend on the molecular gas environment.

[1] Postal address: Institute for Astronomy, University of Hawaii, 2680 Woodlawn Drive, Honolulu, HI 96822; carp@galileo.ifa.hawaii.edu.
[2] Visiting Astronomer, Kitt Peak National Observatory, operated by the National Optical Astronomy Observatory under contract to the National Science Foundation.

In addition to the ^{12}CO and ^{13}CO data from Paper I we have obtained additional data to examine various aspects of the star formation activity in Gem OB1. Searches for dense cores, the precursors to stars, using CS($J = 2$–1) as a tracer were made toward regions with strong ^{13}CO emission. Smaller CS maps were also obtained toward *IRAS* point sources to enable a systematic comparison of core properties and stellar populations. Finally, a near-infrared survey of Sh 247 was conducted to further examine the star forming sites in this region. The details of all of these observations are provided in § 2. In § 3, we discuss the distribution and properties of the dense cores found in the large-scale CS survey, and in § 4, we discuss the distribution of *IRAS* point sources and relate them to both the structure of the molecular gas and the properties of the dense cores. In § 5, we present results of a near-infrared survey, with emphasis on finding enhancements in the stellar surface density and to identify stars with colors characteristic of young stellar objects. We synthesize the results from these various observations and discuss their implications for star formation in the Gem OB1 complex in § 6.

2. OBSERVATIONS AND DATA REDUCTION

2.1. CS($J = 2$–1) *Observations*

The CS($J = 2$–1) (97.98101 GHz) observations were conducted between 1991 December and 1994 February with the FCRAO 14 m telescope using QUARRY (Erickson et al. 1992). QUARRY contains 15 elements arranged in a 3 × 5 grid. The angular spacing of the beams on the sky is 100″ along the short axis of the array and 50″ along the long axis. The data were taken in position-switching mode and calibrated with the standard chopper wheel method of observing an ambient temperature load and sky emission. The spectrometer for each pixel of the array consisted of a 32 channel filter bank with a channel resolution of 250 kHz (0.76 km s^{-1} for CS). The spillover and scattering efficiency ($\eta_{\rm fss}$) of the telescope and radome has been determined from previous measurements to be ~0.7 at these frequencies. A further correction, the source coupling efficiency (η_c), is needed to account for the coupling of the beam to the source. For a uniform source that fills only the main beam of the 14 m telescope, η_c is ~0.7 (i.e., 30% of the power is scattered on angular sizes much greater than the FWHP beam size), while for sources with uniform intensity over a diameter of 30′, η_c is 1.0. The CS emission detected in this survey is typically extended only over a few arcminutes, and so a source coupling efficiency of 0.7 was applied to these data. Antenna temperatures corrected for both the forward scattering and spillover efficiency and the coupling coefficient are denoted as T_R (Kutner & Ulich 1981).

The first stage of the observations consisted of mapping nine large regions with extended bright ^{13}CO emission at 50″ sampling. For eight of these maps, the average rms noise is ΔT_R = 0.24 K, while the remaining map has an rms noise of 0.36 K (see Table 1). In addition, a 4.′2 × 5.′0 region around 58 *IRAS* point sources with far-infrared colors characteristic of young stellar objects (as described in § 4) was mapped at 50″ sampling to an rms noise level of $\Delta T_R \sim 0.14$ K.

2.2. *SQIID*

A 30′ × 45′ area around the Sh 247 H II region covering the region between $6^h5^m20^s \leq \alpha(1950) \leq 6^h7^m24^s$ and $21°15' \leq \delta(1950) \leq 22°$ was observed with SQIID on the 1.3 m telescope at Kitt Peak during two photometric nights in 1993 January with seeing conditions of 1.″5–2″. SQIID observes the *J*, *H*, *K*, and *L* bands simultaneously using four 256 × 256 PtSi arrays. Nonlinearities in the detectors were corrected for using the formulae in the 1993 January SQIID manual. The plate scale of 1.″36 per pixel for each band provided a field of view of 5.′8 × 5.′8 per frame. The observing procedure consisted of observing a 3 × 3 grid with two exposures of 180 s each dithered by 20″ at each position in the grid. The complete observations contained a 2 × 3 mosaic of these grids. The images were reduced in the standard manner with median filtered sky frames and flat fields. Calibration stars were chosen among the fainter standards in the Elias et al. (1982) list and the UKIRT faint standards transformed into the CIT color system (Casali & Hawarden 1992). The observed SQIID colors were consistent with the CIT color system to within ~5% for $J-K \lesssim 1.0$, so no further color corrections were applied. Atmospheric extinction corrections were determined by observing standards over a range of air masses. Stars were identified using DAOFIND and by adding a few additional stars upon visual inspection of the images. Stellar magnitudes were obtained using the IRAF 2.10 version of DAOPHOT on the co-added 3 × 3 grids and point-spread function photometry. The completeness limits of the observations were estimated by adding artificial stars to a test image with the same random noise characteristics as the processed data frames. More than 90% of the stars brighter than 16.1 at *J*, 15.0 at *H*, and 14.5 at *K* were recovered using the DAOFIND task.

TABLE 1

LARGE-SCALE REGIONS MAPPED IN CS($J = 2$–1)

	CENTRAL POSITION (1950)		MAP SIZE ($\alpha \times \delta$)		
REGION	α	δ	arcmin	pc	COMMENTS
1.....	$06^h06^m57^s$	+21°35′	54 × 49	31 × 29	Sh 247
2.....	06 06 48	+20 31	83 × 40	48 × 23	Sh 252
3.....	06 10 27	+17 58	83 × 40	48 × 23	Sh 254–258
4.....	06 11 23	+19 11	37 × 25	22 × 15	BFS 52
5.....	06 10 37	+16 16	41 × 35	24 × 20	...
6.....	05 55 43	+16 19	33 × 40	19 × 23	IRAS 05553+1631
7.....	05 59 57	+16 48	24 × 30	14 × 18	HD 250550
8[a].....	05 57 00	+18 52	43 × 31	25 × 18	...
9.....	05 55 46	+20 13	24 × 20	14 × 12	...

[a] The rms noise of this map is $\Delta T_R = 0.36$ K. The other maps have an rms noise of 0.24 K.

3. MOLECULAR CLOUD CORES

Star formation appears to occur predominantly, if not exclusively, in dense "cores" of molecular gas. A common tracer of dense cores is CS($J = 2$–1), and based on previous CS observations (e.g., Snell et al. 1984), it is expected that the CS emission is tracing H_2 densities of $\gtrsim 10^5$ cm^{-3}. Accordingly, nine regions with strong and extended ^{13}CO emission were mapped in CS($J = 2$–1) as a search for dense molecular material. The positions and sizes of these regions are summarized in Table 1 and are outlined with rectangles in Figure 1. For this study, a cloud core is defined as all regions that contain three or more contiguous pixels that each have an integrated intensity of at least 5 times the rms noise (5 σ). When calculating the properties of the dense core, the total emission within the 3 σ contour level was used. In this manner, 11 cloud cores (see Table 2, top section) were identified in four of the nine areas: near the optical H II regions Sh 247, Sh 252, Sh 254–258, and BFS 52. Contour maps of the integrated CS intensity overlaid on the Palomar Observatory Sky Survey images of Sh 247, Sh 252, and Sh 254–258 are shown in Figures 2–4. A dense core was found a few arcminutes northeast of the BFS 52 H II region but is not shown in these figures. Of these 11 dense cores, nine of them are found along the arcs and filaments described in Paper I. Only cores 4 and 7, two of the lower mass cores found in the CS survey, do not obviously fall into these morphological classifications.

Table 2 (top section) summarizes the properties of the 11 cores found in the large scale CS survey. The table lists the region in which the core is found, the centroid equatorial coordinates, the core mass, and the associated *IRAS* sources. (The *IRAS* source associated with core 5 is slightly beyond the extent of the CS emission in the large-scale survey but is within the boundaries of the CS emission in the deeper, pointed observations of *IRAS* sources described in § 4.) The core masses were calculated assuming that the CS emission is optically thin and in local thermodynamic equilibrium with an abundance relative to molecular hydrogen of 4×10^{-9} (Irvine, Goldsmith, & Hjalmarson 1987) and a kinetic temperature of 10 K. The derived core masses found in the large-scale survey range between 96 $M_\odot$ to 2200 $M_\odot$, where the lower mass range is limited by the sensitivity of the survey.

The total mass contained within these 11 dense cores is 7300 $M_\odot$. The fraction of the mass contained in dense cores to the total molecular mass (see Paper I) varies from 0% to 8% within

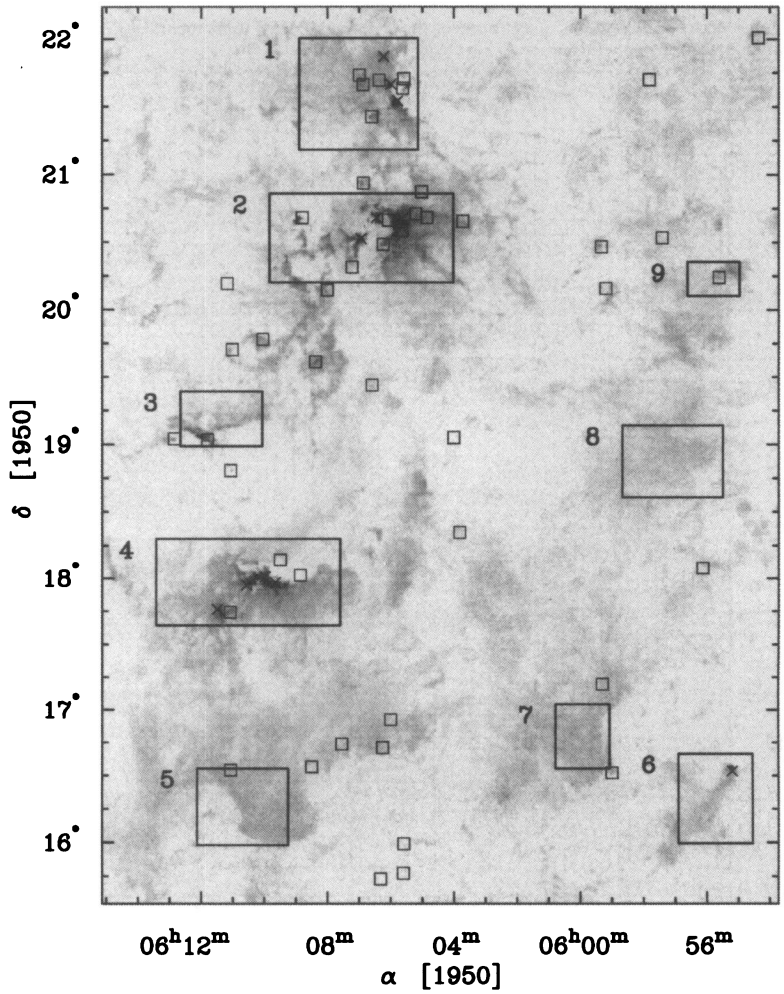

FIG. 1.—Location of regions mapped in CS($J = 2$–1) (*large rectangles*) and *IRAS* point sources with far-infrared colors characteristic of young stellar objects (*small squares* and *crosses*) superposed on an image of the peak ^{12}CO antenna temperature from Paper I. The numbers next to the large rectangles refer to the entries in Table 1. The small squares represent *IRAS* point source with far-infrared luminosities less than 1000 $L_\odot$, while the *crosses* represent *IRAS* point sources more luminous than 1000 $L_\odot$. A 4.2 × 5.0 region was mapped in CS around each of the *IRAS* point sources.

TABLE 2

DENSE CORES IN GEMINI OB1

Identification	Region	R.A. (1950)	decl. (1950)	Mass ($M_\odot$)	*IRAS* Sources
			Large-Scale Survey		
1	Sh 247	06:05:52	21:36:35	1400	06056+2131, 06058+2138, 06062+2140
2	Sh 247	06:06:55	21:41:09	990	06067+2138, 06069+2142
3	Sh 247	06:06:14	21:51:14	310	06061+2151
4	Sh 252	06:05:33	20:27:33	98	...
5	Sh 252	06:05:55	20:30:13	290	06061+2028
6	Sh 252	06:05:38	20:38:16	2200	06055+2039, 06055+2034
7	Sh 252	06:04:49	20:39:49	140	06047+2040
8	Sh 254–258	06:11:27	17:44:56	650	06114+1745, 06110+1744
9	Sh 254–258	06:10:58	17:54:24	300	...
10	Sh 254–258	06:09:59	18:00:12	840	06099+1800
11	BFS 52	06:12:04	19:03:24	96	...
			Pointed Observations		
12	Sh 252	06:06:20	20:40:22	65	06063+2040
13	06096+1757	06:09:40	17:56:54	130	06096+1757
			Additional Cores[a]		
14	05553+1631	05:55:21	16:31:46	13	05553+1631
15	05554+2013	05:55:26	20:13:58	44	05554+2013
16	Sh 254–258	06:10:34	17:57:00	57	06105+1756

[a] The CS emission from these cores does not meet the criteria (see text) to be included in the pointed observations but are likely real detections nonetheless.

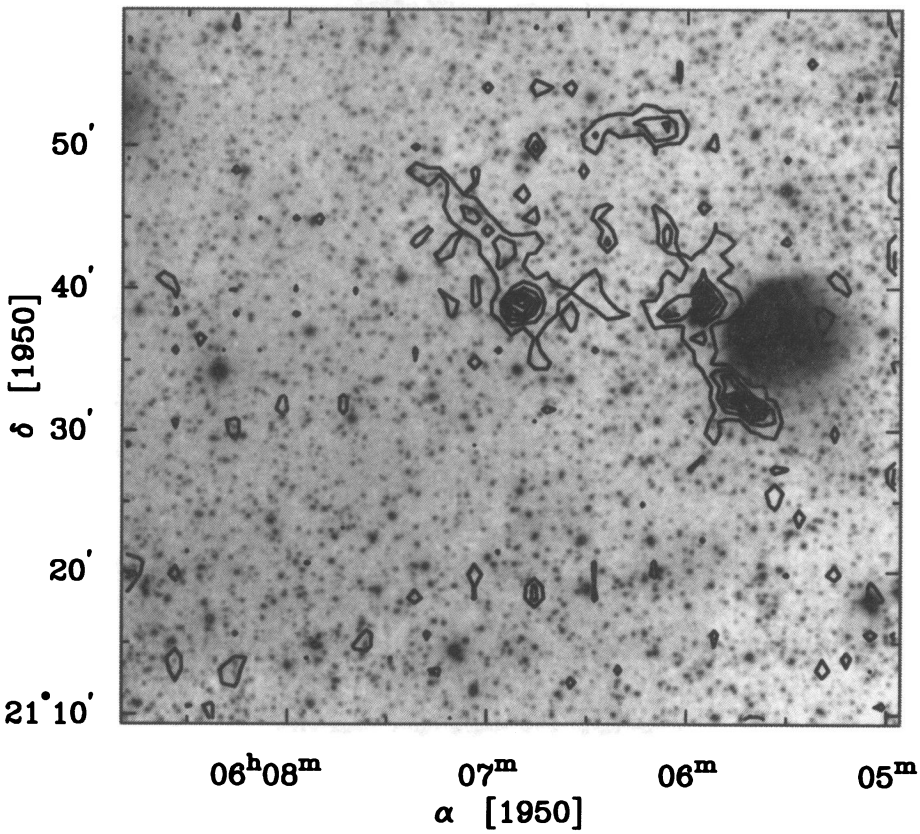

FIG. 2.—Contour map of the integrated CS emission ($\int T_R\,dv$) toward the Sh 247 region overlaid on the red Palomar print. Contour levels begin at 1.9 K km s^{-1} (the 3 σ integrated intensity level) and proceed in increments of 1.9 K km s^{-1}.

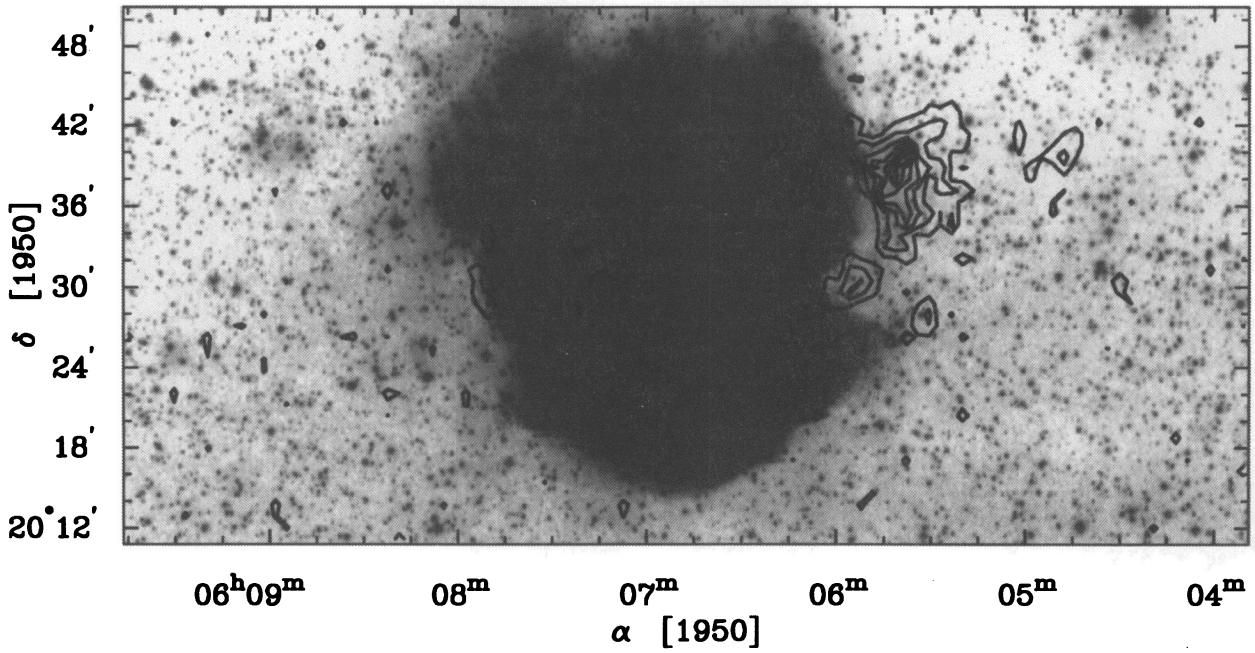

FIG. 3.—Same as Fig. 2, except for the Sh 252 region

the individual regions mapped in CS. For the Gem OB1 complex as a whole, the cores contain 2% of the mass and occupy less than 1% of the total area of the complex. While these values are lower limits since the entire Gem OB1 complex has not been surveyed in CS, we find it extremely unlikely that we have missed a significant mass concentration in massive dense cores in the unsurveyed regions. Evidently, the formation of massive dense cores has involved only a small fraction of the total area and mass of the Gem OB1 complex.

4. *IRAS* POINT SOURCES IN GEMINI OB1

4.1. *Candidate Star-Forming Regions*

The *IRAS* far-infrared survey provides a powerful tool to locate star-forming regions within molecular clouds complexes, as young embedded stars have far-infrared colors distinct from many other sources (see, e.g., Walker et al. 1989). Accordingly, the *IRAS* Point Source Catalog (Joint *IRAS* Science Working Group 1988) was used to identify far-infrared sources with colors characteristic of young stellar objects that lie within the boundaries of the ^{12}CO map of the Gem OB1 cloud complex and then to correlate the properties of the *IRAS* sources with the distribution of dense cores. Figure 5 (*left*) shows a far-infrared color-color diagram for the 60 *IRAS* sources in the Gem OB1 cloud complex that have detections at both 25 and 60 μm and a 60 μm flux density of $S_{60} \geq 3.0$ Jy. These criteria were imposed to insure that these sources were truly stellar objects. The *IRAS* point sources associated with the Herbig Ae/Be star LkHα 208 and the H II region Sh 259

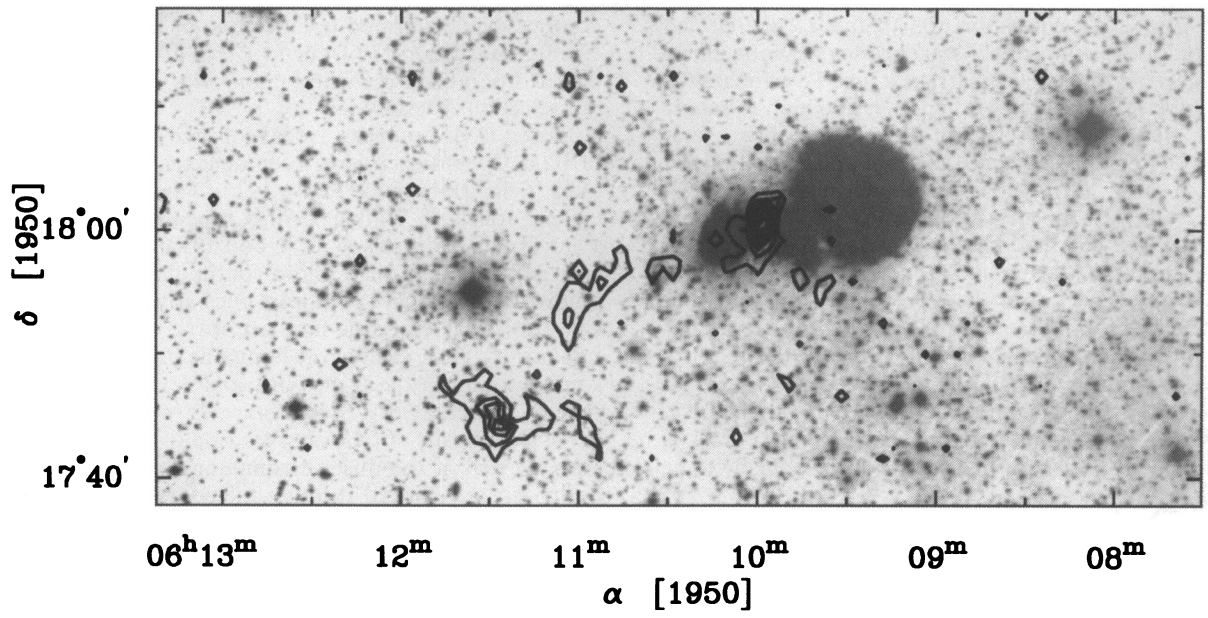

FIG. 4.—Same as Fig. 2, except for the Sh 254–258 region

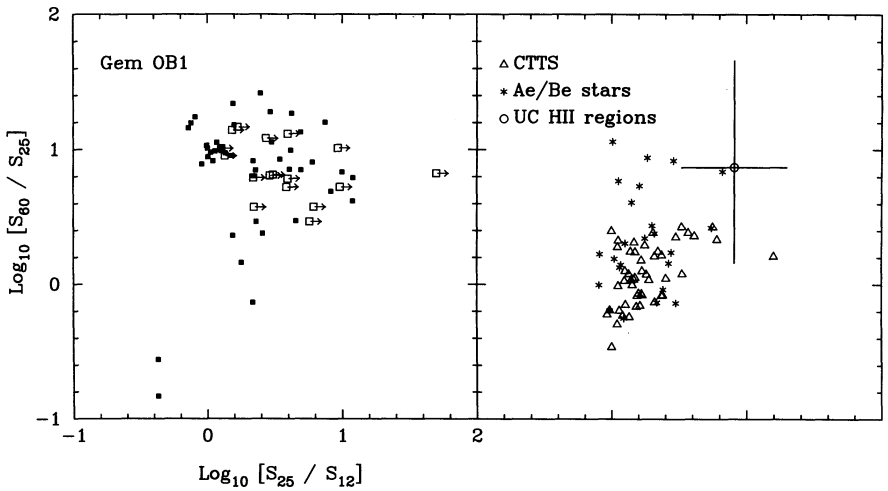

FIG. 5.—(*Right*) Color-color diagram for the 60 *IRAS* point sources in Gem OB1 with 25 and 60 μm detections and a minimum flux density of 3 Jy at 60 μm. The filled squares represent *IRAS* point sources with 12 μm detections, and open squares represent sources with upper limits at 12 μm. (*Left*) The corresponding color-color diagram for T Tauri stars (Strom et al. 1989), Herbig Ae/Be stars (Hillenbrand et al. 1992), and ultracompact H II regions (Wood & Churchwell 1989). All but two of the *IRAS* sources in Gem OB1, selected by the above criteria, have colors characteristic of young stellar objects.

have been omitted since these sources are most likely foreground or background to the Gem OB1 cloud complex (see Paper I). The solid squares in Figure 5 represent *IRAS* point sources with positive detections at 12, 25, and 60 μm, while open squares represent sources with upper limit 12 μm fluxes. Figure 5 (*right*) shows the corresponding color-color diagram for T Tauri stars (Strom et al. 1989), Herbig Ae/Be stars (Hillenbrand et al. 1992), and ultracompact H II regions (Wood & Churchwell 1989). The comparison sources have far-infrared colors of $\log_{10}[S_\nu(25\ \mu m)/S_\nu(12\ \mu m)] \gtrsim 0.0$ and $\log_{10}[S_\nu(60\ \mu m)/S_\nu(25\ \mu m)] \gtrsim -0.4$. All but two of the *IRAS* point sources in the Gem OB1 sample are consistent with these colors. These two sources, which have comparatively blue colors, are associated with a carbon star and a MI supergiant and were removed from the sample. The remaining 58 sources are listed in Table 3. The far-infrared colors of these 58 sources are most consistent with the colors of the more massive stars among the comparison sources.

The largest potential contamination to this *IRAS* selected sample of candidate embedded star-forming regions likely comes from galaxies and galactic cirrus clouds. To estimate the potential number of galaxies bright enough at 60 μm to satisfy the adopted *IRAS* source selection criteria, the fluxes and colors of the *IRAS* sources toward the region centered on the Galactic longitude of 193° (the same as the Gem OB1 complex) and latitude of 21° with an equivalent area to the ^{13}CO map of the Gem OB1 cloud complex were examined. Of the 91 *IRAS* point sources in this control region, none had a flux density at 60 μm in excess of 3 Jy, and therefore contamination from galaxies in the *IRAS* point sources selected in the Gem OB1 complex is likely to be negligible. Furthermore, the requirement of a detection at 25 μm and 60 μm excludes most cirrus-type objects from appearing in this sample (Hacking & Houck 1987). Thus, significant contamination from other sources is unlikely, and the *IRAS* sources listed in Table 3 are likely to be star-forming regions.

Table 3 summarizes the properties of the 58 *IRAS* sources comprising the sample of candidate star forming regions. Column (1) lists the *IRAS* point source name, columns (2)–(5) the observed 12, 25, 60, and 100 μm flux densities, and column (6) the estimated far-infrared luminosity (L_{FIR}). The far-infrared luminosities were obtained by summing the luminosities in the 12, 25, and 60 μm band passes. Explicitly,

$$L_{FIR} = 0.304\left(\frac{D}{\text{kpc}}\right)^2 \sum_i \left[\frac{\text{BW}(\lambda_i)}{10^{12}\ \text{Hz}}\right]\left(\frac{S_{\nu i}}{\text{Jy}}\right) L_\odot\ ,$$

where D is the distance to the source, BW the *IRAS* bandwidths, and S_ν the observed flux densities. The sum extends over the 12, 25, and 60 μm bands. The 100 μm flux densities were not used since in many instances the emission at 100 μm was blended with neighboring sources, and thus the 100 μm luminosities could not be consistently derived for all sources. In addition, upper limits to flux densities at 12 μm were not used. For sources with good 100 μm detections, roughly one-half of the total far-infrared luminosity is radiated in the 100 μm band. Thus the true far-infrared luminosity may be on average twice that listed in Table 3. Figure 6 presents a histogram of the far-infrared luminosities for the 58 *IRAS* sources. The luminosities range from 14 $L_\odot$ to 14,000 $L_\odot$. The lack of detected point sources with luminosities $< 14\ L_\odot$ is a result of our selection criteria.

Eleven *IRAS* sources have far-infrared luminosities in excess of 1000 $L_\odot$ and each have been detected in the radio continuum (Felli, Habing, & Israël 1977; Turner & Terzian 1985; Cohen, Jones, & Walker 1989; Carpenter, Snell, & Schloerb 1990; Kurtz, Churchwell, & Wood 1994). The inferred excitation parameters of these radio continuum sources are consistent with the presence of at least one early OB-type star, which can also provide a large fraction of the observed far-infrared luminosity. Thus, each of the luminous ($L_{FIR} \geq 1000\ L_\odot$) *IRAS* sources found in the Gem OB1 complex probably represents regions forming early B-type stars. In principle, some of the lower luminosity *IRAS* sources could represent high-mass stars as well, if the dust surrounding these objects has been destroyed or removed through the course of the evolution of the star so that the far-infrared luminosity severely underestimates the bolometric luminosity of the source. We assume that this is not the case for the majority of the low-luminosity sources and that these sources generally represent low-

TABLE 3

IRAS POINT SOURCES IN GEMINI OB1

IRAS Source	S_{12} (Jy)	S_{25} (Jy)	S_{60} (Jy)	S_{100} (Jy)	L_{FIR} ($L_\odot$)
05539+2159.....	0.9	1.4	3.2	5.6	34
05553+1631.....	<1.3	63.1	420.7	527.5	1700
05554+2013.....	4.1	34.0	166.8	269.9	820
05561+1804.....	<0.2	1.0	6.0	8.5	25
05572+2031.....	0.4	2.0	6.1	6.6	40
05575+2141.....	<0.2	0.4	6.2	16.6	22
05590+2008.....	0.4	0.9	5.7	23.0	31
05591+1630.....	4.5	9.9	7.3	10.6	170
05591+2027.....	1.1	1.4	14.4	29.4	74
05593+1711.....	0.4	0.5	4.8	13.1	26
06036+2038.....	<0.2	0.6	3.4	20.8	14
06038+1820.....	<0.2	1.0	5.1	6.2	22
06039+1902.....	<0.4	1.0	12.2	27.3	45
06047+2040.....	1.6	6.7	48.1	<92.3	220
06049+2051.....	<0.3	0.4	4.4	<21.3	17
06051+2041.....	0.6	1.3	10.4	15.1	51
06054+2141.....	0.9	0.7	9.8	<66.9	52
06055+2137.....	<0.5	4.4	23.4	<20.7	100
06055+2039.....	15.6	76.8	1032.0	1715.0	4000
06055+2034.....	0.9	3.9	73.0	<1715.0	270
06056+1559.....	0.3	0.4	3.5	15.1	20
06056+1546.....	<0.3	0.4	3.5	<12.4	14
06056+2131.....	48.6	241.3	1708.0	2563.0	7800
06058+2138.....	14.0	140.2	955.5	1666.0	4200
06060+2038.....	2.3	27.1	112.3	<18.4	570
06060+1655.....	1.0	1.6	34.5	70.1	140
06061+2151.....	12.0	144.8	895.6	1130.0	4000
06061+2028.....	2.0	3.2	48.5	211.4	210
06062+2140.....	0.8	2.0	4.8	6.1	42
06062+1642.....	<0.2	1.5	5.8	8.7	28
06063+1543.....	0.4	0.6	5.6	<19.5	29
06063+2040.....	9.7	72.7	1157.0	2045.0	4300
06065+2124.....	1.5	1.8	19.9	54.6	100
06065+1925.....	1.0	1.0	8.6	29.4	50
06067+2138.....	<0.3	2.5	25.6	83.7	96
06067+2055.....	1.4	1.4	14.5	25.5	79
06068+2030.....	13.3	38.8	737.5	1134.0	2800
06069+2142.....	7.7	13.9	20.3	<83.7	290
06071+2018.....	<0.4	0.6	8.1	<47.6	29
06075+1643.....	1.3	3.8	43.2	125.0	180
06079+2007.....	<0.2	0.7	4.7	14.2	19
06083+1936.....	0.8	0.7	5.6	31.0	36
06085+1633.....	0.4	0.6	5.9	15.8	30
06087+2040.....	1.8	1.4	25.1	<107.3	120
06088+1800.....	0.5	0.6	4.6	<26.7	27
06094+1808.....	0.6	0.6	6.2	<16.7	34
06096+1757.....	5.5	13.6	356.4	<5285.0	1300
06099+1800.....	107.2	371.6	3145.0	5285.0	14000
06100+1946.....	<0.2	1.0	12.9	25.9	47
06105+1756.....	8.7	52.2	422.0	642.8	1800
06110+1941.....	0.7	1.5	4.5	<7.6	36
06110+1632.....	<0.2	0.8	5.0	5.4	21
06110+1847.....	1.4	1.0	16.1	68.8	81
06110+1744.....	<0.2	1.4	4.2	33.9	23
06111+2010.....	<0.4	1.0	3.7	<10.7	18
06114+1745.....	13.3	55.2	545.1	704.6	2300
06117+1901.....	4.7	6.4	60.3	<256.4	320
06128+1901.....	0.4	1.0	6.8	<19.5	35

luminosity, low-mass stars. The source IRAS 06039+1902 associated with the B1 emission line star HD 251726 is one possible exception.

4.2. *Spatial Distribution*

Figure 1 shows the spatial distribution of the 58 *IRAS* sources listed in Table 3 superposed on an image of the peak ^{12}CO(J = 1–0) antenna temperature. The point sources have been arbitrarily divided into two luminosity bins: those with

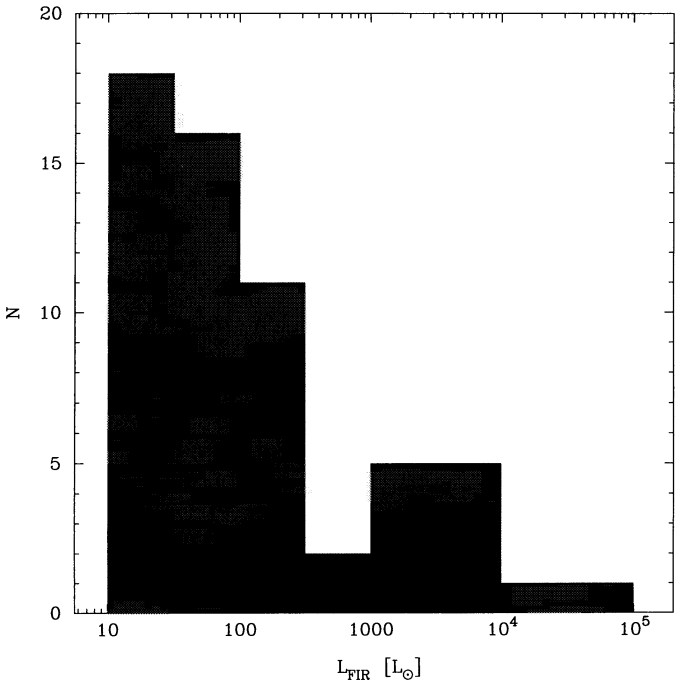

FIG. 6.—Histogram of the far-infrared luminosities of the 58 *IRAS* point sources in the Gem OB1 complex that have far-infrared colors characteristic of embedded star-forming regions (see Table 3). The turnover at faint luminosities represents the sensitivity and confusion limits of the *IRAS* survey. The lack of *IRAS* sources with luminosities $\lesssim 14\ L_\odot$ is due to our selection criteria.

$L_{FIR} < 1000\ L_\odot$ (*small squares*) and those with $L_{FIR} \geq 1000\ L_\odot$ (*crosses*). Six of the *IRAS* sources are located several arcminutes away from any ^{12}CO emission. Of these five sources, one (IRAS 06039+1902) is associated with the B1 emission line star HD 251726, three others (IRAS 06056+1546, 06056+1559, 06056+1543) are projected against the optical boundaries of the Sh 261 H II region, one (IRAS 06088+1800) is projected against Sh 254, and the final source (IRAS 06111+2010) has no association with another optically visible object. The nature of these objects is unclear but will nonetheless remain in the sample.

Comparison of the spatial distribution of luminous *IRAS* sources (Fig. 1) with the spatial distribution of dense cores (Figs. 2–4) indicates that the signatures of massive star formation—optical H II regions, luminous far-infrared sources, and radio continuum emission—are clustered in the Gem OB1 cloud complex. Of the 11 *IRAS* point sources with $L_{FIR} \geq 1000\ L_\odot$, 10 are located in the general vicinity of the Sharpless H II regions Sh 247, Sh 252, and Sh 254–258. Only IRAS 05553+131, located at one end of a filament in the southwest corner of the Gem OB1 complex, has a far-infrared luminosity in excess of 1000 $L_\odot$ and is not adjacent to an optical H II region. The less luminous sources are more widespread throughout the Gem OB1 cloud complex.

4.3. *Association of IRAS Point Sources with Dense Cores*

4.3.1. *Targeted* CS *Survey*

A 4.′2 × 5.′0 CS map was made around each of the 58 *IRAS* point sources in order to make a systematic comparison of the core properties. These maps are slightly more sensitive than the large-scale maps presented in § 3. Figure 7 displays a mosaic of the small-scale CS integrated intensity maps for the

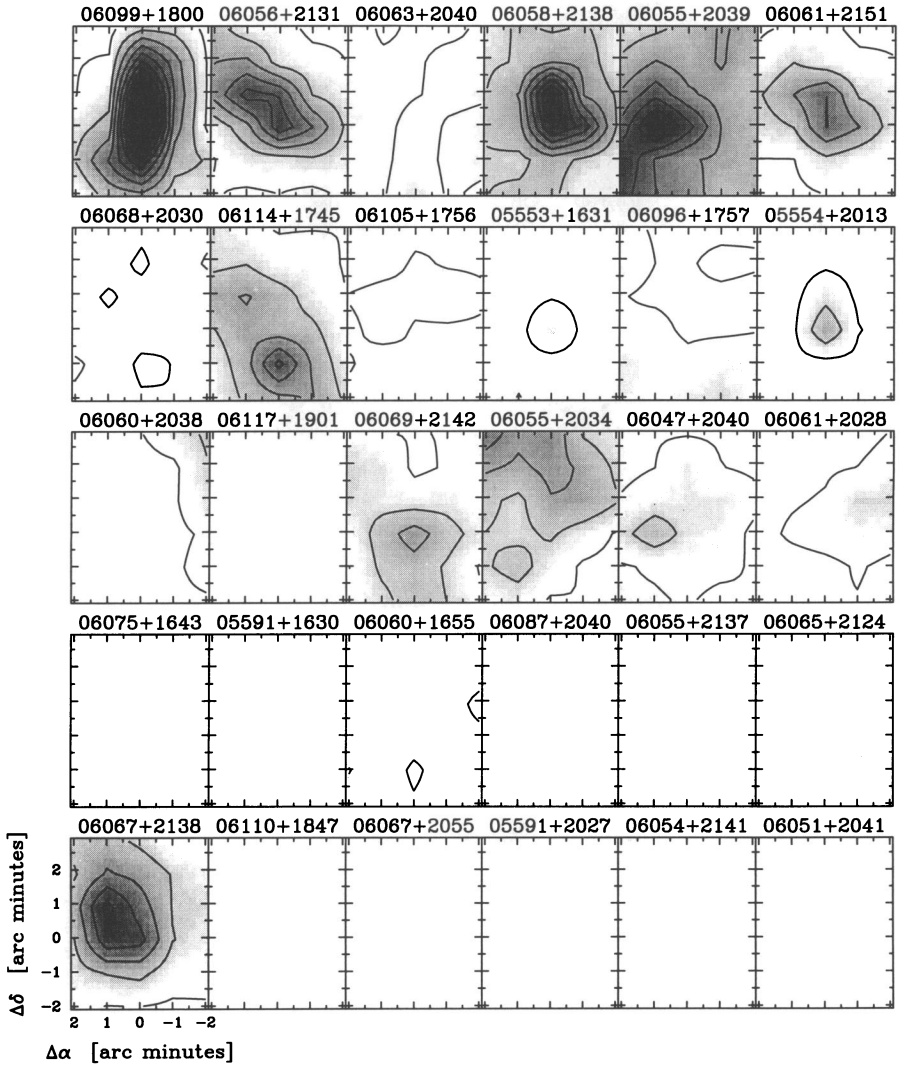

FIG. 7.—Contour maps of the integrated CS($J = 2$–1) intensity toward the 30 most luminous *IRAS* sources in Gem OB1. The *IRAS* sources are displayed in decreasing luminosity order, with the most luminous source (06099+1800) in the upper left-hand corner. Contour levels are the same for each map and begin at $\int T_R\,dv = 1.13$ K km s^{-1} with increments of 2.26 K km s^{-1}. Of the 28 *IRAS* sources mapped in CS but not shown here, two have a CS detection at or above the 3 σ noise level (see text).

30 most luminous *IRAS* sources in the Gem OB1 complex, shown in order of decreasing far-infrared luminosity starting in the upper left-hand corner. Of the 28 *IRAS* sources not shown, CS emission was detected only near sources IRAS 06062+2140 and 06110+1744. To facilitate comparison between the sources, the contour/halftones for each map in Figure 7 begin at the 3 σ noise level ($\int T_R\,dv = 1.13$ K km s^{-1}) with increments of 2 σ (2.26 K km s^{-1}). The (0, 0) positions in these maps refer to the respective *IRAS* point-source positions. Adopting the same definition of a dense core described in § 3, although using the appropriate noise levels for these smaller maps, we identify cores in 16 of the 58 *IRAS* sources. The emission detected in most of these regions is associated with the same cores already identified in the large-scale survey (see Table 2, top section), as only two new cores were detected in the targeted CS observations. Both of these new cores are found in the regions mapped in the large-scale CS survey but were previously not detected owing to the lower sensitivity of that survey. The properties of these two cores are listed in Table 2 (middle section). In addition, we identity three regions with CS emission that did not meet the formal criteria to be classified as a core but are likely real detections nonetheless. For completeness, we list the properties of these three cores in Table 2 (bottom section).

Examination of the CS survey of *IRAS* point sources indicates that the more luminous *IRAS* sources are generally associated with more massive cores (see Table 2). There are exceptions, however, as several luminous *IRAS* sources are associated with relatively low mass cores or were not detected in CS at all despite containing strong ^{12}CO emission (see the discussion below). The lowest luminosity source with a positive CS detection is IRAS 06110+1744, with a far-infrared luminosity of 20 $L_\odot$. The CS emission toward this source, however, peaks toward adjacent luminous *IRAS* sources ($L_{\rm FIR} > 3000$ $L_\odot$) with a massive, extended CS core. A similar situation holds for IRAS 06062+2140. The lowest luminosity *IRAS* source that is centrally located within a CS core is IRAS 06067+2138, which has a far-infrared luminosity of 100 $L_\odot$.

Note, however, that this core is part of a more extended CS emitting region that includes the point source IRAS 06069+2142, which has a far-infrared luminosity of 290 $L_\odot$.

The lack of strong CS emission around some of the more luminous *IRAS* sources is somewhat surprising, as the current paradigm is that all star formation occurs in dense cores. A possible explanation is that the core mass was initially much larger than what is currently observed, but the core has been dispersed by H II regions and stellar winds produced by the young embedded stars. Carpenter et al. (1993) speculated that this was the case for several of cores in their study of luminous *IRAS* sources, some of which are in the Gem OB1 cloud complex, based on dynamical timescales of associated molecular outflows, the morphology of the cores, and the number and characteristics of embedded stars. In fact, the luminous *IRAS* sources not associated with strong CS emission tend to be optically visible H II regions, which one would expect if the surrounding material has largely been dispersed.

4.3.2. *Large-Scale* CS *Survey*

The last column in Table 2 lists the *IRAS* point sources associated with the dense cores. Of the 11 dense cores found in the large-scale survey (see Table 2, top section), eight of them contain an *IRAS* point source within the projected area of the CS emission. Among the three cores without associated *IRAS* sources, core 11 is only a few arcminutes from BFS 52 and the *IRAS* point source 06117+1901, and it is unclear whether this represents a "starless" core or the remains of a once larger core associated with IRAS 06117+1901. In addition, core nine is associated with a nebulous object of unknown nature (Petrossian 1985). Thus, at least 73%, and possibly as many as 90%, of the cores more massive of than $\sim 100\ M_\odot$ appear to be associated with star formation.

5. DISTRIBUTION AND PROPERTIES OF YOUNG STARS

The relatively poor angular resolution of the *IRAS* survey prevents a detailed analysis of the stellar content of the star-forming regions in the Gem OB1 complex, since it is likely that the "point" sources do not represent single stars. The higher angular resolution near-infrared observations with SQIID permit such studies while maintaining the ability to detect embedded star formation sites. In this section, the SQIID data are analyzed with the goal of providing an independent assessment of the embedded stellar content in the Sh 247 region and to further determine how the distribution of the embedded stars correlates with the structure and properties of the molecular gas. The analysis begins by first identifying regions with enhanced stellar surface density and then by finding individual stars with near-infrared colors characteristic of young stellar objects.

5.1. *Clusters*

Figure 8 displays the SQIID K-band mosaic of the Sh 247 region. To search for possible stellar density enhancements in this image, a map of the stellar surface density was created by counting the number of stars between magnitudes $K = 9.0$ and 14.5 within a square aperture and moving this aperture in step sizes of half the aperture width over the full spatial extent of the SQIID image and dividing by the area of the aperture. An aperture size of 1′ was chosen in order to match the typical angular sizes of the dense cores, and in practice, the results described below do not change substantially for different aperture sizes.

Identifying statistically significant stellar density enhancements requires quantifying the expected distribution of surface densities for a random group of stars. For a first-order approximation, the number of observable background and foreground stars was assumed to be constant over the region mapped with SQIID. While dust in the Gem OB1 complex preferentially dims background stars in selected areas, the expected fluctuations in the K-band extinction over the region imaged with SQIID based on the column densities computed in Paper I are typically ~ 0.3 mag and presumed to be negligible for the level of this analysis. Figure 9 shows a histogram of the observed frequency distribution of stellar surface densities in the SQIID mosaic. The solid curve in this figure represents the best-fit Poisson distribution to the observed stellar surface densities. For stellar densities $\lesssim 5$ stars (arcmin)$^{-2}$, the observed stellar density distribution is fairly well approximated by a Poisson distribution with an average stellar surface density of 1.86 stars (arcmin)$^{-2}$. The number of observed regions with higher stellar surface densities, however, exceeds the number expected from a random distribution of stars.

A contour map of the stellar surface density is shown overlaid on the K-band image in Figure 8. The contours begin at 5.95 stars (arcmin)$^{-2}$ (3 σ above the average stellar surface density) with subsequent levels incremented by 5.95 stars (arcmin)$^{-2}$. The background surface density and the statistical significance of higher surface densities were computed using the observed average stellar surface density of 1.86 stars (arcmin)$^{-2}$ and Poisson statistics for a $1' \times 1'$ size counting box. To reduce the number of random groupings of stars in the list of stellar surface density enhancements, only those regions enclosed by a 1 σ contour level and that contain at least a 5 σ enhancement in the total number of stars above the stellar background level were counted as stellar surface density enhancements. The formal confidence limit that these stellar density enhancements do not result from a random grouping of stars is $>99.9\%$. Henceforth, these stellar surface density enhancements are referred to as clusters in anticipation that these regions represent a group of stars in a localized region of space. This does not imply, however, that the stars in these clusters formed at the same time or will remain a bound group.

Table 4 summarizes the properties of the four clusters identified in this manner, including the coordinates of the cluster center, an estimate of the number of stellar members, the cluster radius, and any identification of the cluster with an *IRAS* source. These properties are tabulated for both the 1 σ and 3 σ contour levels to provide some indication on how the cluster properties vary with radius. Subclustering was detected in clusters 1 and 4 at the 3 σ contour level, and we separately tabulate their properties in Table 4. The number of stars in each cluster was estimated by counting the total number of stars within the appropriate contour level and subtracting off the expected number of background/foreground stars based on the average stellar surface density. The uncertainties in the number of stars are the 1 σ errors from counting statistics of the background population. The cluster radius, R, is defined as the radius of a circle that contains the same area as that encompassed by the appropriate contour level. Statistically, the four clusters in the Sh 247 region contain a total of 224 stars brighter than $K = 14.5$ mag within the 1 σ contour boundary. The actual cluster membership is likely to be considerably higher given the finite sensitivity and resolution of the survey. In addition, we have probably overcompensated for the contamination of background stars since, as shown below,

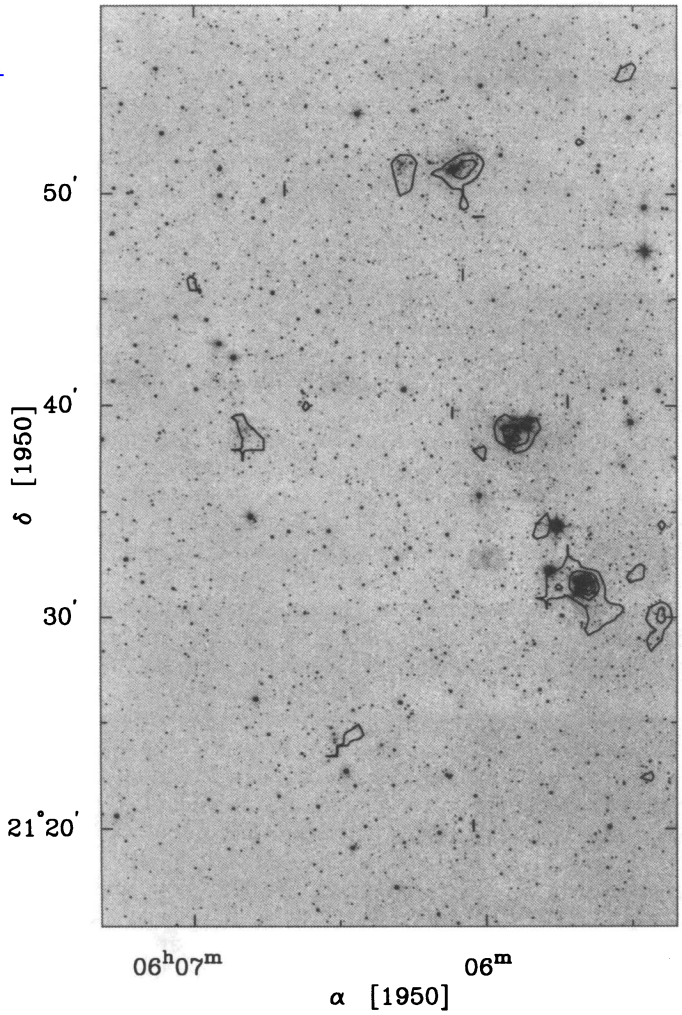

FIG. 8.—The SQIID K-band mosaic of the Sh 247 region overlaid with contours of the stellar surface density for stars with magnitudes of $9.0 \leq m_K \leq 14.5$). The counting was done in a square box 1′ in size and sampled every 30″. The mean surface density is 1.86 stars (arcmin)$^{-2}$ (see Fig. 9). The contours begin at a 3 σ surface density level of 5.95 stars (arcmin)$^{-2}$, with increments of 5.95 stars (arcmin)$^{-2}$.

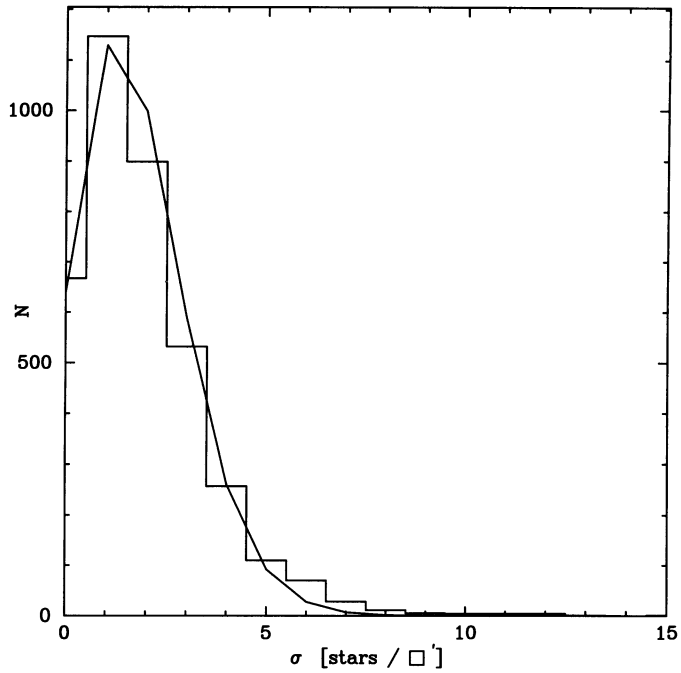

FIG. 9.—Histogram of the stellar surface densities within a 1′ square counting box. The solid line is the best-fit Poisson distribution to the observed stellar surface density distribution. The inferred mean density from the Poisson fit is 1.86 stars (arcmin)$^{-2}$. The surface density distribution below 5 stars (arcmin)$^{-2}$ is well approximated by a Poisson distribution, but there is an excess of higher stellar surface densities compared to the Poisson fit. We identify these regions as potential clusters.

these clusters are associated with high extinction regions that will obscure most background stars.

Figure 10 shows enlargements of the K-band image of each cluster overlaid with a contour map of the integrated CS emission. All four clusters are embedded within a CS dense core and are associated with an *IRAS* point source, although cluster 4 extends considerably beyond the cloud core. This further indicates that these four clusters do indeed represent stars physically related in a localized region. Figure 11 shows the cumulative K-band luminosity functions of the four clusters for stars within the 1 σ boundary. The K-band luminosity functions for clusters 1 and 4 are rather similar; while cluster 2 appears to contain relatively more bright stars, and cluster 3 contains relatively fewer bright stars. The lack of bright stars in cluster 3 is unlikely to be a result of extinction since the H_2 column density through the cores containing the other clusters is similar or larger than the column density through the core containing cluster 3. A Kolmogorov-Smirnov test (Press et al. 1992) was used to quantify the significance of these differences in the luminosity functions. Using the 1 σ level as the cluster boundary, the apparent excess of bright stars in cluster 2 relative to clusters 1 and 4 is not statistically significant, but the probability that cluster 3 contains the same luminosity as the

TABLE 4

STAR CLUSTERS NEAR SH 247

Cluster Number	α (1950)	δ (1950)	Number of Stars 3 σ	Number of Stars 1 σ	R[a] 3 σ	R[a] 1 σ	*IRAS* Source
1a.....	06h06m17s	+21°50′55″	10 ± 2	56 ± 5	0.43	1.22	06061+2151
1b.....	06 06 05	+21 50 54	23 ± 3		0.66		
2	06 05 54	+21 38 53	23 ± 2	33 ± 3	0.59	0.80	06058+2138
3	06 06 50	+21 38 30	16 ± 3	21 ± 3	0.57	0.80	06067+2138
4a.....	06 05 41	+21 31 21	57 ± 4	114 ± 7	0.93	1.74	06056+2131
4b.....	06 05 25	+21 30 01	11 ± 2		0.49		

[a] Cluster radius in parsecs (see text for definition).

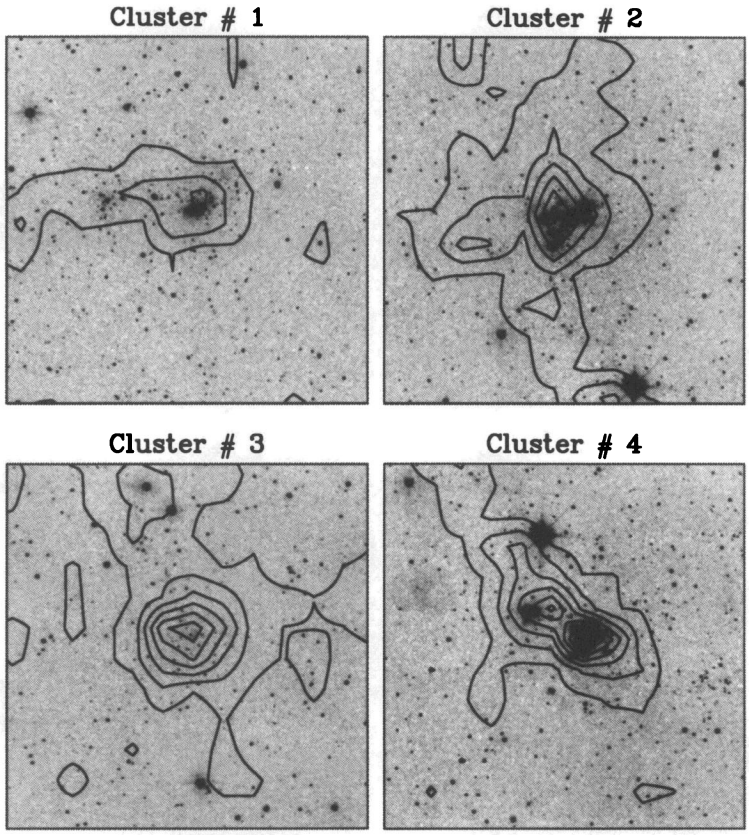

FIG. 10.—Enlargements of the SQIID *K*-band image mosaics around the four identified clusters overlaid with contours of the CS integrated intensity. The contour levels begin at 1.9 K km s^{-1} with increments of 1.9 K km s^{-1}.

other three clusters is between 12% and 38%. This represents the maximum probability since the background/foreground stars have not been subtracted, which will make the clusters appear more alike than they truly are. The probability that the cluster 3 luminosity function is the same as the others decreases to $\lesssim 5\%$ if we use the 3 σ contour level to define the clusters and hence reduce the foreground/background contamination. We conclude that these differences in the luminosity functions are likely real, which might indicate variations in the age of the clusters (Zinnecker, McCaughrean, & Wilking 1993), the mass function, or accretion rates. Each of these scenarios is plausible, and spectroscopic observations of the embedded stars are needed to ascertain the relative importance of these effects.

Clusters 1, 2, and 4 are each associated with a luminous *IRAS* source ($L_{\rm FIR} > 1000\ L_\odot$) and compact radio continuum emission. Thus, the enhanced far-infrared luminosity is due both to the large number of stars and the presence of at least one early B-type star. At first glance this provides further evidence that most, if not all, high-mass stars form in clusters and not in isolation. However, no clusters were found associated with the Sh 247 H II region, which is excited by an early B-type star (Hunter & Massey 1990). Zinnecker et al. (1993) noted a similar situation for the optical H II regions Sh 255 and Sh 257 and the cluster associated with the luminous source IRAS 06099+1800, and they suggested that the birth function of stellar masses can vary dramatically from one region to another in that B stars can form either in isolation or in a cluster.

This suggestion by Zinnecker et al. (1993), however, leads to unsettling consequences for the star formation history of the Gem OB1 cloud complex. Assuming for the moment that the formation of single, isolated, early B-type stars has occurred in at least three (Sh 247, Sh 255, Sh 257) of the eight optical H II regions in the Gem OB1 complex, then this mode of star formation must be fairly common. Corresponding near-infrared data for the other five optical H II regions (Sh 252, Sh 254, Sh 256, Sh 258, and BFS 52) are not available, although optically Pismis (1970) found a cluster of 65 stars distributed over a 8 pc size region in Sh 252. Thus, if the 11 luminous *IRAS* sources represent an earlier evolutionary stage than the B stars associated with the extended optical H II regions, then roughly 40% of these *IRAS* sources (i.e., four of them) should be forming a single B-type star under this hypothesis. Of these 11 sources, seven have been observed in the near-infrared, and *all* contain a cluster of stars (see above and also Carpenter et al. 1993; McCaughrean 1993; Zinnecker et al. 1993). In addition, Carpenter et al. (1993) surveyed 21 luminous *IRAS* sources in the *J*, *H*, and *K* bands, and of the 17 sources with a massive star as evidenced by radio continuum emission (three of which are in the Gem OB1 complex), all contain a cluster of stars to some degree. Therefore, while none of the three optical H II regions in the Gem OB1 complex that have been observed in the near-infrared contain a statistically significant cluster of stars, all of the luminous *IRAS* sources that have been imaged do. The notion that these regions represent extreme variations in the stellar birth function could only explain these observations if the star formation process has changed with time.

As an alternative hypothesis, we suggest that the single

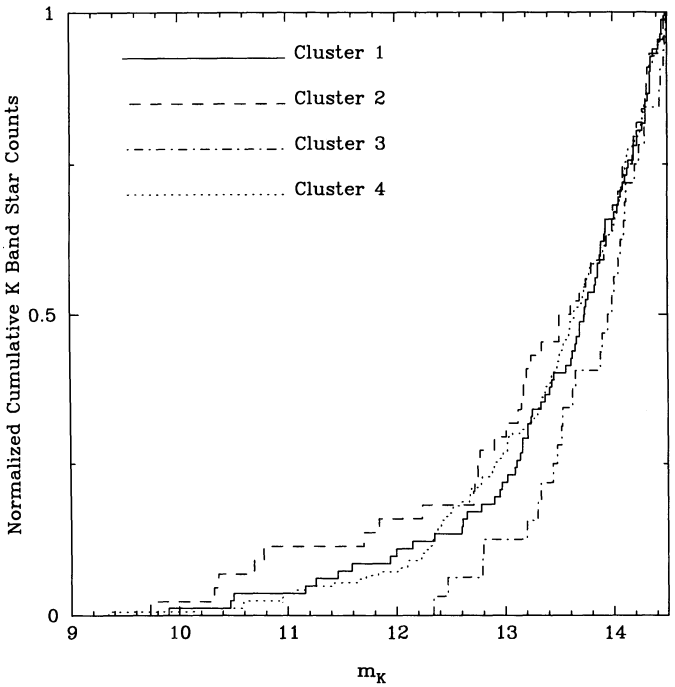

FIG. 11.—Cumulative K-band luminosity functions for the four clusters identified in the SQIID K-band image at the 1 σ contour level (see Table 4) normalized by the total number of stars within that contour. The normalization constants for clusters 1–4 are 82, 44, 32, and 166 stars, respectively. Note that the data have not been binned in presenting these histograms, and that background/foreground stars have not been removed.

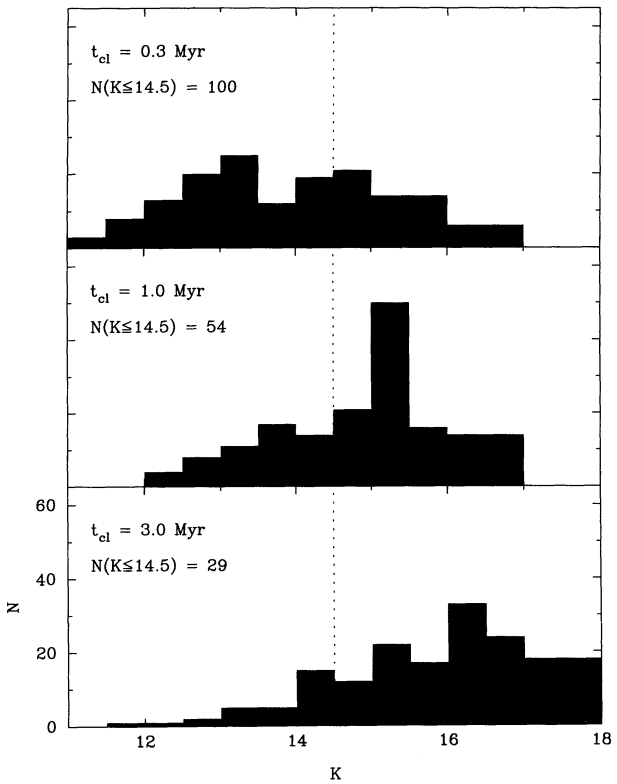

FIG. 12.—This figure shows the time evolution in the K-band luminosity function for a hypothetical cluster at a distance of 2.0 kpc that has a Miller-Scalo initial mass function. The dashed line shows the completeness limit of the SQIID data. Note that disk accretion and extinction have not been included in these calculations. As the cluster evolves with time, fewer stars will be detectable. We suggest that this luminosity evolution along with dynamical evolution of the clusters is responsible for the lack of stars observed around several of the optical H II regions in the Gem OB1 complex.

OB-type stars in the optical H II regions were initially part of a cluster that is no longer discernible as such because the stars have largely dispersed and have become fainter with time. The extent of the radio continuum emission, the molecular outflow timescales, and the ubiquity of outflows and stars with excess near-infrared emission (see § 5.2 and Carpenter et al. 1993) suggest that the deeply embedded *IRAS* sources are younger than the stars in the optical H II regions. Figure 12 shows the evolution of the K-band luminosity for a cluster over the age range of 0.3 Myr to 3.0 Myr. The stellar masses in this hypothetical cluster were drawn from a Monte Carlo simulation of the Miller-Scalo initial mass function (Miller & Scalo 1979), and the K magnitudes were computed using the pre–main-sequence evolution tracks of D'Antona & Mazzitelli (1994; see also Meyer et al. 1995). Stellar masses between 0.10 to 2.5 $M_\odot$ are included in these models. Accretion and extinction are not considered and, in any event, will partially offset each other in terms of visibility of a star at near-infrared wavelengths. The lowest mass star visible at $K = 14.5$ is $\sim 0.25\ M_\odot$ for a cluster age of 0.3 Myr and $\sim 0.9\ M_\odot$ for 3 Myr. Figure 12 shows that a 0.3 Myr old cluster containing 100 stars brighter than $K = 14.5$ will have 54 stars brighter than $K = 14.5$ at an age of 1.0 Myr and 29 stars brighter than $K = 14.5$ at an age of 3.0 Myr. Thus, luminosity evolution can drastically reduce the visibility of clusters, but alone it is not sufficient to account for the lack of prominent clusters around some of the optically visible H II regions.

In addition to luminosity evolution, a cluster will likely disperse as it emerges from the molecular cloud core in which it formed. According to the cluster evolution models by Lada, Margulis, & Dearborn (1984), a cluster of ~ 100 stars will disperse over a region ~ 2 pc in radius in a few million years assuming that the star formation efficiency is $\lesssim 30\%$, as commonly inferred. After considering the effects of luminosity evolution as described above, the estimated observed stellar surface density of this hypothetical cluster after a few million years would be $\lesssim 1$ star per square arcminute, which is below the stellar surface density limit used to identify the clusters listed in Table 4. While the actual stellar ages and initial stellar populations are unknown, and there may indeed be statistically significant variations in the stellar birth function among these star-forming regions, our results suggest that cluster dispersal and luminosity evolution can account for the lack of visible, high-density clusters around the extended optical H II regions without invoking *extreme* variations in the stellar birth function.

5.2. *Excess Near-Infrared Emission*

Numerous investigations have shown that young stellar objects have infrared emission in excess of what is expected from its photosphere (see, e.g., Strom et al. 1989). This "excess" infrared emission can be explained by invoking various combinations of circumstellar disks and envelopes (Adams, Lada, & Shu 1987), and so young stars can potentially be identified by this excess infrared emission. Such a search was conducted using the near-infrared photometry of stars in Sh 247 by constructing a $J-H$ versus $H-K$ color-color diagram and by

identifying stars with colors inconsistent with reddened main-sequence and giant stars, such as Herbig Ae/Be stars and classical T Tauri stars. It should be noted that many young stars could have circumstellar material and not show a signature of a near-infrared excesses if the excess is small or appears primarily at longer wavelengths.

Figure 13*a* shows the color-color diagram for the 1859 stars in the Sh 247 region that have J, H, and K magnitudes brighter than 16.5, 15.5, and 14.5, respectively, and have estimated color errors less than or equal to 0.15 mag. An additional 412 stars have $K \leq 14.5$ but do not satisfy the J- and H-band magnitude or color error criteria. The solid curves in Figure 13*a* denote the expected positions of unreddened main-sequence and giant stars, and the dotted line shows the slope of the reddening vector (Cohen et al. 1981). Many of the stars in the field imaged have colors consistent with K, G, and F main-sequence stars and giant stars, and another large group of objects have colors of main-sequence and giant stars reddened by 5–10 mag of visual extinction. The third significant group of stars seen in Figure 13*a* has colors inconsistent with reddened main-sequence or giant stars.

Without the benefit of a control field to compare with the observations of Sh 247, we have simulated the $J-H$ versus $H-K$ color-color diagram for a population of field stars to determine to what extent the scatter seen in the stellar colors in Figure 13*a* is due to the presence of young stars with infrared excesses. The distribution of field stars was generated using a Monte Carlo simulation of the Bahcall-Soneira (Bahcall & Soneira 1980) model of the Galaxy kindly provided by T. Jarrett (Jarrett 1992). The extinction assigned to each star included the standard visual extinction-distance relation of 1 mag kpc^{-1} and dust associated with the Sh 247 molecular cloud (see Paper I). Noise was added to the J-, H-, and K-band magnitudes based on Poisson counting statistics appropriate for the SQIID observations. Figure 13*b* shows the results of the simulation for stars brighter than $J = 16.5$, $H = 15.5$, and $K = 14.5$. Qualitatively, the simulation agrees well with the observations in the distribution of stars around the unreddened main sequence, the scatter blueward of the main sequence, and the number of highly reddened stars. The most significant difference between the simulation and the observations is the larger number of observed stars that lie to the right of the locus of reddened main-sequence and giant stars. These stars most likely have excess near-infrared emission.

The simulation was used as an aid in estimating the number of stars in the Sh 247 region with near-infrared excesses. This was done by comparing the number of stars with colors suggestive of excess near-infrared emission in the Sh 247 region (643 stars) and the simulation (294 stars). In Sh 247, this sample of stars contains both stars with intrinsic near-infrared excesses and stars with apparent excesses caused by random noise. The simulation, of course, contains no stars with intrinsic excess near-infrared emission. Statistically then, 349 of the 1859 stars in Sh 247 with J, H, and K detections have intrinsic excess near-infrared emission and are likely pre–main-sequence objects. This is comparable to the number of stars determined to be in clusters in this region (§ 5.1), suggesting that clusters are a prominent part of the current star formation activity in this region.

The simulation provides a test in determining the appropriate selection criteria to select an uncontaminated set of infrared excess stars. By requiring that the perpendicular distance between the stellar colors and the reddening vector exceed 3 times the uncertainty in the stellar colors, 99% of the candidate near-infrared excess stars in the simulation were removed. A similar criteria removed >99% of the stars blueward of the main sequence and giant stars in the color-color diagram. We therefore adopted the 3 σ criteria, which yielded a sample of 99 stars that likely have excess near-infrared emission. The spatial distribution of these 99 stars is shown in Figure 14. The stars are divided into two groups: the open circles signify stars with $J-H$ colors of ≤ 0.6, and filled squares signify redder sources. This distinction is made since the stars with $J-H$ colors $\lesssim 0.6$ are the most likely group to still be contaminated by nonexcess

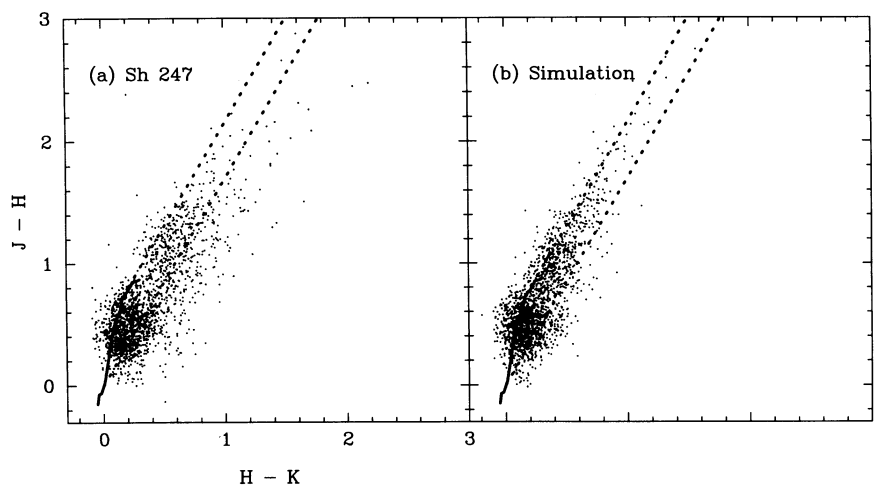

FIG. 13.—(*Right*) The $J-H$ vs. $H-K$ color-color diagram for the 1859 stars in Sh 247 with color errors less than 0^m.15 and J-, H-, and K-band magnitudes brighter than 16.5, 15.5, and 14.5, respectively. The solid lines denote the expected colors of unreddened main-sequence and red giants stars transformed into the CIT color system (Bessell & Brett 1988), and the dotted lines show the reddening vectors measured in the CIT color system by (Cohen et al. 1981). (*Left*) A simulation of the expected appearance of the color-color diagram created using a Monte Carlo star count model of the Galaxy and the observed extinction. Random noise was added to the individual magnitudes in a manner consistent with the observed errors. Evidently the simulation can account for many of the features in the observed color-color diagram, except for the excess number of stars with extremely red $J-H$ and $H-K$ colors. We identify these stars as likely pre–main-sequence objects with excess near-infrared emission.

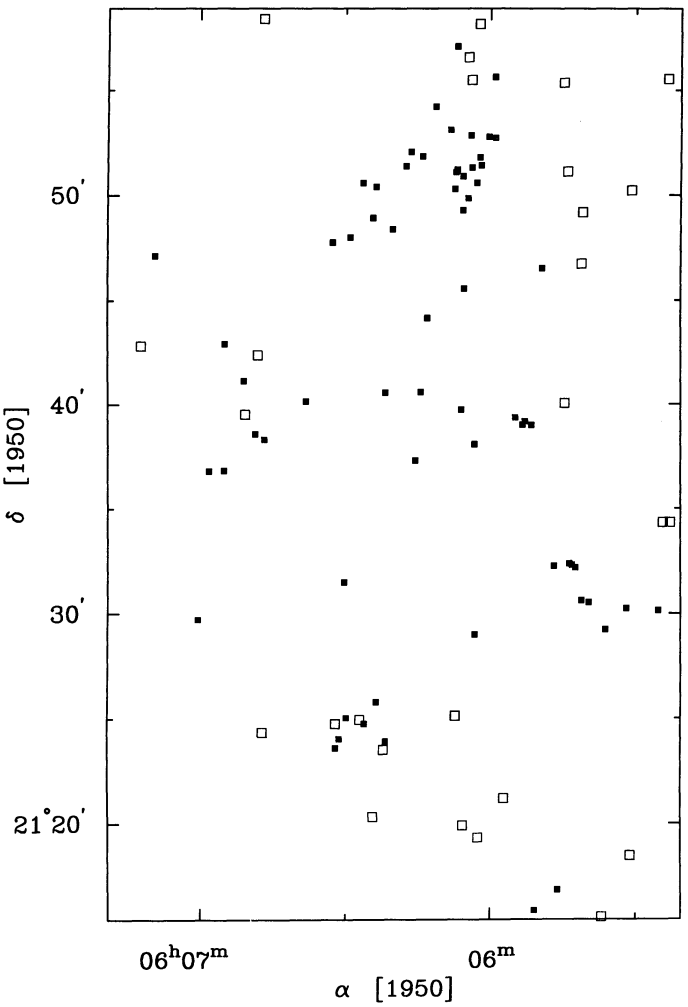

FIG. 14.—The spatial distribution of the 99 stars that have $J-H$ and $H-K$ colors that deviate by at least 3 σ from the reddening vector and hence likely have near-infrared excesses. The solid squares denote stars with $J-H$ colors redder than 0.6, and open squares denote the bluer stars. This distinction is made since the latter sample is the most likely still to be contaminated by stars without true infrared excesses. A small grouping of stars with near-infrared excesses not identified in the stellar surface density map is apparent near (α, δ) = (6^h30^m, 21°25′) and is associated with the *IRAS* point source 06065+2124.

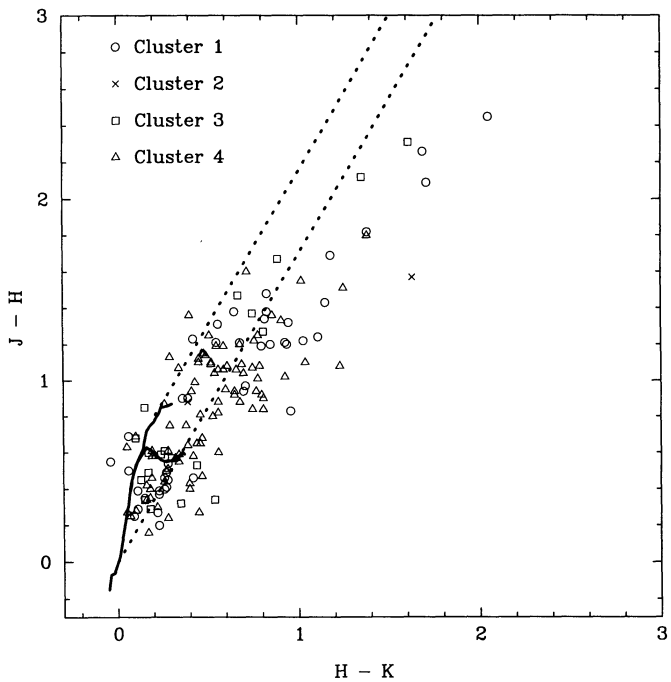

FIG. 15.—Color-color diagram for the stars found within the 1 σ cluster boundary. Only stars with J-, H-, and K-band magnitudes brighter than 16.5, 15.5, and 14.5, respectively, and with color errors less than 0.15 are included in this figure.

stars due to the sheer number of objects around the unreddened main sequence and giant branch. Based on the observed J magnitudes and $J-H$ colors, most of the stars with near-infrared excesses likely have masses $\lesssim 1\ M_\odot$ (Meyer et al. 1995).

Figure 14 shows that the distribution of stars with near-infrared excesses is not randomly distributed throughout the Gem OB1 cloud complex. The largest concentration of stars with infrared excesses is near cluster 1 (IRAS 06061+2151). The distribution of these stars extends beyond the formal boundaries of the cluster themselves since the extent of the clusters can only be measured to a finite surface density level. The other clusters do not contain a high concentration of stars with infrared excesses, but this is likely a result of these stars not being visible at J band. Close inspection of Figure 14 also reveals a small grouping of seven to nine stars with near-infrared excess near (α, δ) = (6^h30^m, 21°25′). This grouping is associated with the point source IRAS 06065+2124, which has a far-infrared luminosity of $\sim 100\ L_\odot$, and a dense core detected in HCO^+ but not CS (see § 3 and Kömpe et al. 1989). Thus, between the star counts and the spatial distribution of stars with near-infrared excesses, five clusters of stars have been identified, all of which are associated with a core detectable in either CS and HCO^+.

Finally, we investigate the fraction of stars in the clusters identified with the stellar surface density map (see § 5.2) that have near-infrared excesses. Figure 15 shows the color-color diagram for those stars that have J-, H-, and K-band magnitudes brighter than 16.5, 15.5, and 14.5, respectively, with color errors less than 0.15 and are found within the four clusters as defined by the 1 σ stellar surface density limit. Not surprisingly, Figure 15 shows that these four clusters contain some of the redder stellar objects in the Sh 247 region. To establish a lower limit to the number of cluster stars with near-infrared excesses, we ignore the presence of foreground and background stars and simply compute the fraction number of stars that are found to the right of the rightmost reddening vector. While we showed in Figure 13 that stars with normal stellar colors can populate this region of the color-color diagram owing to random photometric noise, inspection of Figure 15 suggests that the number of stars with intrinsic excess near-infrared emission is comparable to the number of stars with normal stellar colors. Therefore, to first order, photometric noise will not preferentially create the appearance of stars with near-infrared excesses since random noise will also make some stars with intrinic near-infrared excesses appear like normal reddened stars. Based on this assumption, we establish a lower limit to the near-infrared excess fraction of $\gtrsim 50\%$ for the stars shown in Figure 15. Some of the stars in Figure 15 are undoubtedly background or foreground to the clusters, and based on the average stellar surface density observed in the Sh 247 region, we expect a total of ~ 100 such stars contained

within the four cluster boundaries. However, Galactic star count models suggest that roughly half of these stars will be background to the dense cores in which the clusters are embedded and will be obscured by the large amounts of dust expected to be associated with these cores. Therefore, an upper limit to the number of stars in these clusters with near-infrared excesses is ~74%. Evidently, these clusters contain a substantial number of stars with near-infrared excesses, which supports the assertion that they are indeed rather young objects.

6. SYNTHESIS: THE FORMATION OF DENSE CORES AND EMBEDDED CLUSTERS

The large-scale CS survey indicated that dense cores are sparsely distributed, and in terms of mass, only ~2% of the total molecular gas of the Gem OB1 complex is contained in dense cores defined by CS emission. The dense gas is associated with high column density material [$N(H_2) \gtrsim 10^{22}$ cm^{-2}; see Paper I], indicating that these high column density regions represent volume density enhancements as well. In Paper I, we suggested that these high column density regions have been formed by expanding H II regions and stellar winds since they are often found in arc-shaped structures and, in a few instances, appear directly related to optical H II regions. This interpretation implies that the dense cores also formed during this process, and the fact that the CS emission is often elongated along these arc-shaped structures (see Figs. 2–4) supports this assertion. We suggest, therefore, that currently, one of the prominent mechanisms for forming massive concentrations of dense gas (more than a few hundred solar masses) in the Gem OB1 complex is by sweeping up and compressing the low-density molecular material.

The notion that the winds and expanding H II regions from OB stars can form dense cores by sweeping up molecular material was explored in detail by Elmegreen & Lada (1977). In their model, the molecular gas swept up by an expanding H II region will remain stable against gravitational collapse by the external pressure from the ionized gas until the gas column density exceeds a critical value. In the following discussion, we compare the predictions of this model with the observed properties of the Sh 252 region. Grasdalen & Carraco (1975) estimate an age of ~2 Myr for the cluster of stars associated with the H II region, and we assume that the exciting star for the nebula (an O6.5 star) has the same age. If the dense gas surrounding the western edge of the Sh 252 formed as a result of an expanding H II region as we suggest, than the timescale to sweep up the molecular material, create the dense gas, and form a cluster of stars is roughly a couple of million years. Since most of the ionization in Sh 252 is provided by a single star, we assume that the pressure decreases as a function of time and radius in a manner appropriate for an expanding H II region (Spitzer 1978). We find, then, that the swept-up gas around Sh 252 will be stable against gravitational collapse until the column density perpendicular to the shell exceeds $\sim 3 \times 10^{22}$ cm^{-2}. Unfortunately, the Sh 252 shell is observed primarily edge on, and therefore, any estimate of the column density perpendicular to the shell is necessarily model dependent. Assuming that the shell has an inner radius of 8–9 pc and a finite thickness of ~2 pc, we find that the observed column density along the shell is about 6 times the column density perpendicular to it. Thus, since the observed column densities along the shell are typically $2–3 \times 10^{22}$ cm^{-2} with a maximum value of 6.4×10^{22} cm^{-2} where the stellar cluster is forming, the observed column densities are in rough agreement with the predicted critical column densities needed to form a gravitational instability in a swept-up shell. Moreover, the predicted timescale to develop dense cores and form stars within the swept-up material is ~3 Myr (Elmegreen & Lada 1977), which is in rough agreement with the inferred cluster age given the observational and modeling uncertainties. We conclude, therefore, that the observed properties of the Sh 252 region are consistent with the notion that the dense core and the embedded cluster of stars were formed during the expansion of the H II region. A similar conclusion was reached by Lada & Wooden (1979) in their study of the Sh 252 region, and in fact, similar conclusions have been reached in a number of regions, including W3, Cep OB3, and Orion among others (see review by Elmegreen 1992).

Such a detailed comparison between observations and theories cannot be made for the other H II/core regions since the necessary age estimates are not available. Furthermore, not all of the cores are found adjacent to optical H II regions, and so expanding H II regions obviously cannot account for every observed dense core and cluster. However, the essential feature of the Elmegreen & Lada (1977) model may be operative, namely, that the massive cores have been formed by external compression of the molecular gas, which would explain the arc and filamentary structures in which the cores are generally found. Stellar winds and cloud-cloud collisions, for example, are other processes that can lead to compression of the gas. This is in contrast to "spontaneous" star formation described by Shu, Adams, & Lizano (1987), in which a dense core forms more slowly and without an external stimulus. In the Gem OB1 complex, our observations suggest that induced star formation is a more prominent mechanism to form masive cores (and subsequently stellar clusters). Lower luminosity sources, and presumably lower mass cores (see discussion below), are found scattered throughout the Gem OB1 complex. It is unclear from our data as to whether these sources have formed by "spontaneous" means or by the external compression of the molecular gas. We note, however, that the low-luminosity *IRAS* sources are not preferentially found along the arcs and filaments in the molecular gas as are the high-luminosity *IRAS* sources.

The dense cores are likely to be the formation sites of the next generation of stars in the Gem OB1 complex, and indeed, *IRAS* point sources, radio continuum objects, and clusters have been identified in most of the cores. The correspondence of compact radio continuum objects with luminous *IRAS* sources suggests than we can use the far-infrared luminosity as a crude tracer of the embedded stellar content, in that all luminous *IRAS* sources are sites of massive star formation, while the low-luminosity *IRAS* sources represent sites of low-mass star formation. With this assumption we find that the low-luminosity and low-mass stars are generally not detected in CS (see § 4.3.1). We suggest that the lack of CS detection toward these sources primarily reflects that the cores associated with these sources are below the mass sensitivity limit of the CS survey (~100 $M_\odot$), and in fact, the molecular mass estimated from the ^{12}CO and ^{13}CO data in Paper I within the 4.2 × 5.0 region mapped in CS around the *IRAS* sources is generally below 100 $M_\odot$. This implies that massive stars are associated with more massive cores. It is not clear from our data if this is an environmental effect or if a massive star merely has a greater statistical probability of forming given that more dense gas is present. The global trend between luminosity and core mass is not perfect, however. Several rather luminous objects

are not associated with strong CS emission, and as argued in § 4.3.1, this may indicate that these cores are being dispersed. In general, we suggest that time evolution of cores and stellar clusters contributes significantly to the observed properties of the gas and stars (see §§ 4.3.1 and 5.2).

Surprisingly, a large fraction of the cores already appears to contain star formation. Of the 11 dense cores found in the large scale CS survey, at last eight, and possibly 10, are associated with star formation (see § 4). Three of these cores are observed in our near-infrared imaging survey of Sh 247, and all three contain a high surface density of stars (§ 5.2). Other cores in the Gem OB1 complex that have been observed at near-infrared wavelengths (see, e.g., Hodapp 1994) also contain a high stellar surface density. Unless these cores are the last generation of star formation in the Gem OB1 complex, which we find highly unlikely given the substantial amount of molecular material still remaining, this suggests that star formation occurs quickly after a *massive* dense core is created. This in turn implies that if star formation is to continue, then massive dense cores must continually be formed over the lifetime of the Gem OB1 complex, and that the distribution and number of dense cores were not fixed at the time the Gem OB1 complex was formed. As discussed above, one mechanism to continually form massive dense cores that appears to be important in the Gem OB1 complex is the sweeping up of molecular material by the expansion of compact H II regions, a process more commonly referred to as "triggered" star formation.

This work was supported by NSF grant AST 91-15721 to the Five College Radio Astronomy Observatory. This research has made use of the SIMBAD database, operated at CDS, Strasbourg, France, J. M. C. acknowledges support from the James Clerk Maxwell Telescope Post Doctoral Fellowship while this manuscript was in preparation.

REFERENCES

Adams, F. C., Lada, C. J., & Shu, F. H. 1987, ApJ, 312, 788
Bahcall, J. N., & Soneira, R. M. 1980, ApJS, 44, 73
Bessell, M. S., & Brett, J. M. 1988, PASP, 100, 1134
Carpenter, J. M., Snell, R. L., & Schloerb, F. P. 1990, ApJ, 362, 147
———. 1995, ApJ, 445, 246 (Paper I)
Carpenter, J. M., Snell, R. L., Schloerb, F. P., & Skrutskie, M. F. 1993, ApJ, 407, 657
Casali, M., & Hawarden, T. 1992, The UKIRT/JMCT Newsletter No. 4, 33
Cohen, J. G., Grogel, J. A., Perrson, S. E., & Elias, J. H. 1981, ApJ, 249, 481
Cohen, M., Jones, B. F., & Walker, H. J. 1989, ApJ, 341, 908
D'Antona, F., & Mazzitelli, I. 1994, ApJS, 90, 467
Elias, J. H., Frogel, J. A., Matthews, K., & Neugebauer, G. 1982, AJ, 87, 1029
Elmegreen, B. G. 1992, in Star Formation in Stellar Systems, ed. G. Tenorio-Tagle, M. Prieto, & F. Sanchez (Cambridge: Cambridge University Press), 381
Elmegreen, B. G., & Lada, C. H. 1977, ApJ, 214, 725
Erickson, N. R., Goldsmith, P. F., Novak, G., Grosslein, R. M., Viscuso, P. J., Erickson, R. B., & Predmore, C. R. 1992, IEEE Trans. Microwave Theory and Techniques, 40, 1
Felli, M., Habing, H. J., & Israël, F. P. 1977, A&A, 59, 43
Grasdalen, G. L., & Carrasco, L. 1975, A&A, 43, 259
Hacking, P., & Houck, J. R. 1987, ApJS, 63, 311
Hillenbrand, L. A., Strom, S. E., Vrba, F. J., & Keene, J. 1992, ApJ, 398, 613
Hodapp, K.-W. 1994, ApJS, 94, 615
Hunter, D. A., & Massey, P. 1990, AJ, 99, 846
Irvine, W. M., Goldsmith, P. F., & Hjalmarson, A. 1987, in Interstellar Processes, ed. D. L. Hollenbach & H. A. Thronson, Jr. (Dordrecht: Reidel), 561
Jarrett, T. H. 1992, Ph.D. thesis, Univ. of Massachusetts
Joint *IRAS* Science Working Group. 1988, *IRAS* Point Source Catalog, Version 2 (Washington: GPO)
Kömpe, C., Joncas, G., Baudry, A., & Wouterloot, J. G. A. 1989, A&A, 221, 295
Kurtz, S., Churchwell, E., & Wood, D. O. S. 1994, ApJS, 91, 659
Kutner, M. L., & Ulich, B. L. 1981, ApJ, 250, 341
Lada, C. J., Margulis, M., & Dearborn, D. 1984, ApJ, 285, 141
Lada, C. J., & Wooden, W. 1979, ApJ, 232, 158
Lada, E. A., Bally, J., & Stark, A. A. 1991a, ApJ, 368, 432
Lada, E. A., DePoy, D. L., Evans, N. J. II, & Gatley, I. 1991b, ApJ, 371, 171
Lada, E. A., Strom, K. M., & Myers, P. C. 1993, in Protostars and Planets, ed. E. H. Levy & J. I. Lunine (Tucson: Univ. of Arizona Press), 245
McCaughrean, M. 1993, in Massive Stars: Their Lives in the Interstellar Medium, ed. J. P. Cassinelli & E. B. Churchwell (ASP Conf. Ser., 35), 80
Meyer, R. M., Carpenter, J. M., Hillenbrand, L. A., Strom, S. E., & Dougados, C. 1995, AJ, submitted
Miller, G. E., & Scalo, J. M. 1979, ApJS, 41, 513
Petrossian, V. M. 1985, Astrofizika, 22, 423
Pismis, P. 1970, Bol. Obs. Tonanzintla y Tacubaya, 5, 219
Press, W. H., Teukolsky, S. A., Vetterling, W. T., & Flannery, B. P. 1992, Numerical Recipes (Cambridge: Cambridge Univ. Press)
Shu, F. H., Adams, F. C., & Lizano, S. 1987, ARA&A, 25, 23
Snell, R. L., Mundy, L. G., Goldsmith, P. F., Evans, N. J. II., & Erickson, N. R. 1984, ApJ, 276, 625
Spitzer, L., Jr. 1978, Physical Processes in the Interstellar Medium (New York: Wiley)
Strom, K. M., Strom, S. E., Edwards, S., Cabrit, S., & Skrutskie, M. F. 1989, AJ, 97, 1451
Turner, K. C., & Terzian, Y. 1985, AJ, 90, 59
Walker, H. J., Cohen, M., Volk, K., Wainscoat, R. J., & Schwartz, D. E. 1989, AJ, 98, 2163
Wood, D. O. S., & Churchwell, E. 1989, ApJ, 340, 265
Zinnecker, H., McCaughrean, M. J., & Wilking, B. A. 1993, in Protostars and Planets III, ed. E. H. Levy & J. I. Lunine (Tucson: Univ. of Arizona Press), 429